An Improved Time Interpolation for Three-Dimensional Doppler Wind Analysis

SHUN LIU

Department of Atmospheric Science, Lanzhou University, Lanzhou, Gansu, China, and Cooperative Institute for Mesoscale Meteorological Studies, University of Oklahoma, Norman, Oklahoma

CHONGJIAN QIU

Atmosphere Department, Lanzhou University, Lanzhou, Gansu, China

QIN XU

National Severe Storms Laboratory, Norman, Oklahoma

PENGFEI ZHANG

Cooperative Institute for Mesoscale Meteorological Studies, University of Oklahoma, Norman, Oklahoma

(Manuscript received 11 November 2003, in final form 9 April 2004)

ABSTRACT

A temporal interpolation is required for three-dimensional Doppler wind analysis when the precise measurement time is counted for each radar beam position. The time interpolation is traditionally done by a linear scheme either in the measurement space or in the analysis space. Because a volume scan often takes 5–10 min, the linear time interpolation is not accurate enough to capture the rapidly changing winds associated with a fast-moving and fast-growing storm. Performing the linear interpolation in a frame moving with the storm can reduce the error, but the analyzed wind field is traditionally assumed to be stationary in the moving frame. The stationary assumption simplifies the computation but ignores the time variation of the true wind field in the moving frame. By incorporating a linear time interpolation into the moving frame wind analysis, an improved scheme is developed. The merits of the new scheme are demonstrated by idealized examples and numerical experiments with simulated radar observations. The new scheme is also applied to real radar data for a supercell storm.

1. Introduction

Modern Doppler radars have the ability to scan large volumes of the atmosphere at high space and time resolution. High-resolution radar measurements have provided unprecedented opportunities for high-resolution weather analyses, and many different types of methods have been developed in recent years to analyze and retrieve high-resolution wind fields from radar-observed winds. Among the existing methods, the least squares methods are relatively simple and often very efficient in comparison with the adjoint method (Sun and Crook 1994, 1996; Xu et al. 1994, 2001). Various least squares methods have been widely used for three-dimensional wind analyses (Scialom and Lemaître 1990; Laroche and Zawadzki 1994; Shapiro et al. 1995; Qiu and Xu 1996; Zhang and Gal-Chen 1996; Gao et al. 1999; Liou 1999; Weygandt et al. 2002). When the methods are used for three-dimensional wind analyses at a single time level, radar wind measurements at different beam positions (and, thus, different times) have to be either assumed as instantaneous for the entire volume scan or interpolated to the analysis time. In the latter case, two successive volume scans have to be available, and only those collocated or approximately collocated measurements from the two volume scans can be used for the time interpolation (at collocated measurement points). Traditionally, the time interpolation is done by a linear method either in the measurement space (Clark et al. 1980; Protat and Zawadzki 1999, 2000) or in the analysis space (Liu and Qiu 2003). Because a volume scan often takes 5–10 min, the linear time interpolation may not be accurate enough to capture the rapidly changing winds associated with a fast-moving and/or fast-growing storm. Thus, it is necessary to improve the time interpolation method, and this is the motivation of this study.

There are many time interpolation methods that are more accurate than the linear one, but they all require more than two time levels of observations and thus can-

Corresponding author address: Dr. Qin Xu, National Severe Storms Laboratory, 1313 Halley Circle, Norman, OK 73069.
E-mail: qin.xu@noaa.gov

not be used when only two successive volume scans are available. The true wind time variations are associated with two processes: the storm advection and the storm evolution (growth or decay in a frame moving with the storm). The advection-caused time variation can be reduced as well as the advection-caused error if the analysis is performed in a moving frame following the storm as proposed by Gal-Chen (1982). For well-organized storm systems, the merits of using a moving frame have been demonstrated both numerically and analytically in many studies (Chong et al. 1983; Yang and Xu 1996; Zhang and Gal-Chen 1996; Caillault and Lemaître 1999; Liou 1999, 2002). It is necessary to point out that selecting a moving frame is not always trivial (Matejka 2002) and often involves some uncertainty regarding its optimality. For poorly organized or scattered storms, the concept of a moving frame becomes even meaningless. When a moving frame is applied to real Doppler radar data collected for a well-organized storm system, the analyzed wind field is traditionally assumed to be stationary in the moving frame so that sequentially dislocated measurements can be used together to improve the three-dimensional wind analysis in the moving frame. In this case, because the storm evolution is ignored in the moving frame, the true storm evolution can cause another type of error, called evolution-caused error, in the moving-frame wind analysis. The task of this study is to reduce the evolution-caused error in a moving-frame wind analysis by using two successive radar volume scans.

Clearly, if the analysis is extended into the time dimension, then both temporal and spatial interpolations can be easily performed in the analysis space. Such an extension was recently made by Liu and Qiu (2003) but was applied only to a fixed frame. This paper will further extend their method to three-dimensional wind analyses in a moving frame. As in Liu and Qiu (2003), the analyzed wind field will be expressed by a linear time interpolation between two analytical fields expressed by Legendre polynomial expansions in three spatial dimensions at the beginning time of the first volume scan and the ending time of the second volume scan. The Legendre polynomial expansions are as in multiple analytical Doppler (MANDOP; Scialom and Lemaître 1990; Tabary and Scialom 2001), but with the three-dimensional analysis domain in a moving frame. As will be demonstrated in this paper, this extension can reduce the evolution-caused error and thus improve the time interpolation. The method is introduced as a combination of the traditional moving-frame method and the extended method of Liu and Qiu (2003) in the next section. The merits of the combined method are illustrated by idealized examples in section 3 and then further demonstrated by numerical experiments with simulated radar observations in section 4. This method is applied to real radar data in section 5. Conclusions follow in section 6.

2. Methodology and formulations

In this paper, the traditional three-dimensional variational (3DVAR) data assimilation method is extended to estimate the wind fields (u, v, w) from two volume scans of Doppler radar radial wind observations by minimizing the following cost function:

$$J = J^{\mathrm{CON}} + J^{B} + J^{O}, \tag{1}$$

where J^{CON} is the weak-form mass continuity constraint, J^{B} is the weak-form boundary constraint, and J^{O} measures the distance between observed and analyzed radial winds. The forms of J^{CON} and J^{B} used in this paper are the same as in Scialom and Lemaître [1990, see their (23) and (27)]. The specific form of J^{O} is given by

$$J^{O} = (\mathbf{a} - \mathbf{o})^{\mathrm{T}}\mathbf{W}(\mathbf{a} - \mathbf{o}), \tag{2}$$

where $\mathbf{a} = [v_r^a(\mathbf{x}_m, t_m) | m = 1, 2, \ldots M]$ is the state vector of the analyzed radial wind field, $\mathbf{o} = [v_r^o(\mathbf{x}_m) | m = 1, 2, \ldots M]$ is the observation vector composed of two successive volume scans, and $\mathbf{W}$ denotes the weight matrix for which a diagonal form is used in this paper. Here, $v_r^a(\mathbf{x}, t)$ denotes the analyzed radial wind field that is a continuous function of $(\mathbf{x}, t) = (x, y, z, t)$. The subscript m denotes the sequence of radar measurements in four-dimensional space $(\mathbf{x}, t)$, the mth measurement point is denoted by $(\mathbf{x}_m, t_m)$, and $M = M_1 + M_2$, where M_1 and M_2 are the numbers of measurements in the first and second volume scans, respectively.

In this paper, the analytical form of $v_r^a(\mathbf{x}, t)$ is given by a linear time interpolation between two Legendre polynomial expansions in three spatial dimensions (see appendix A): one is at the beginning time ($t = t_1$) of the first volume scan and other is at the ending time ($t = t_M$) of the second volume scan. The state vector of the analyzed radial wind field in the measurement space of the two volume scans at the beginning $t = t_1$ can be denoted by $\mathbf{a}_1 = [v_r^a(\mathbf{x}_m, t_1) | m = 1, 2, \ldots M]$. As shown in appendix A [(A6)], this vector can be related to the coefficients of the Legendre polynomial expansion by

$$\mathbf{a}_1 = \mathbf{L}\mathbf{c}_1, \tag{3}$$

where $\mathbf{L}$ is the measurement matrix determined by the measurement space and the truncated Legendre polynomial expansion in $\mathbf{x}$, and $\mathbf{c}_1$ is the vector composed of the coefficients of the Legendre polynomial expansion at $t = t_1$. Similarly, the state vector of the analyzed radial wind field in the measurement space at the ending time $t = t_M$ can be denoted by $\mathbf{a}_2 = [v_r^a(\mathbf{x}_m, t_M) | m = 1, 2, \ldots M]$. This vector can be related to the coefficients of the Legendre polynomial expansion at $t = t_M$, that is,

$$\mathbf{a}_2 = \mathbf{L}\mathbf{c}_2. \tag{4}$$

After the above preparations, the analyzed radial wind at $(\mathbf{x}, t) = (\mathbf{x}_m, t_m)$ can be obtained by the following linear time interpolation:

$$v_r^a(\mathbf{x}_m, t_m) = \alpha_1 v_r^a(\mathbf{x}_m, t_1) + \alpha_2 v_r^a(\mathbf{x}_m, t_M), \quad (5)$$

where

$$\alpha_1 = \frac{t_M - t_m}{t_M - t_1} \quad \text{and} \quad \alpha_2 = \frac{t_m - t_1}{t_M - t_1}. \quad (6)$$

Because the time interpolation is performed in analysis space, it does not require that the measurements from the two volume scans be collocated. Applying the linear time interpolation in (5) to all the observation point yields the following expression for the state vector in (2):

$$\mathbf{a} = T(\mathbf{a}_1, \mathbf{a}_2). \quad (7)$$

Substituting (7) into the observation term in (2) gives

$$J^o = [T(\mathbf{L}\mathbf{c}_1, \mathbf{L}\mathbf{c}_2) - \mathbf{o}]^{\mathrm{T}} \mathbf{W} [T(\mathbf{L}\mathbf{c}_1, \mathbf{L}\mathbf{c}_2) - \mathbf{o}]. \quad (8)$$

The goal of the analysis is to determine coefficients $\mathbf{c}_1$ and $\mathbf{c}_2$ by minimizing the cost function. In this cost function, as shown in (3)–(8), because the analyzed winds are interpolated to the observation points in space and time (by using the basis function expansions and linear time interpolation), the method is not affected by the time–space distributions of the observed radial winds. When this formulation is used in a fixed frame, only the evolution-caused error can be reduced effectively as explained in the introduction. This approach is called the evolution correction (EC) method. Without this evolution correction, $v_r^a(\mathbf{x}_m, t_1)$ and $v_r^a(\mathbf{x}_m, t_M)$ become identical, and so do $\mathbf{c}_1$ and $\mathbf{c}_2$. In this case, vector $\mathbf{a}$ reduces to the simple form in (A6) and the method reduces to the traditional no-correction (NC) method.

The EC method cannot reduce the advection-caused error effectively, unless the analysis is performed in a moving frame. The speed of this moving frame, denoted by u_0 and v_0, can be estimated from the movement of the concerned main reflectivity pattern. In this moving frame, $v_r^a(\mathbf{x}_m, t_m)$ is replaced by $v_r^a(\mathbf{x}'_m, t_m)$, where $\mathbf{x}' = (x', y', z)$ denotes the moving-frame coordinate system that is related to the fixed frame coordinates by

$$x' = x - u_0(t - t_1) \quad \text{and} \quad (9)$$

$$y' = y - v_0(t - t_1). \quad (10)$$

Assume that the analyzed radial wind field is stationary in the moving frame, then $v_r^a(\mathbf{x}'_m, t_1) = v_r^a(\mathbf{x}'_m, t_m) = v_r^a(\mathbf{x}'_m, t_M)$ becomes independent of time and thus can be expressed by the same expansion of Legendre polynomial basis functions as in appendix A, but in the moving frame (instead of the fixed frame). In the moving frame, the state vector of the analyzed radial wind field is given by $\mathbf{a} = [v_r^a(\mathbf{x}'_m, t_1) | m = 1, 2, \ldots M]$ in the measurement space. As in (A6), but in the moving frame, this vector can be related to the coefficients of the Legendre polynomial expansion by

$$\mathbf{a} = \mathbf{L}'\mathbf{c}, \quad (11)$$

where $\mathbf{L}'$ is the measurement matrix in the moving frame, which is similar to $\mathbf{L}$ in (A7) but obtained by substituting (9)–(10) into (A4). In the moving frame, the radar positions are no longer fixed but are functions of time, so $\mathbf{L}'$ is a matrix function of time. This is different from the original MANDOP (see appendix A). Substituting (11) into the observation term in (2) gives

$$J^o = (\mathbf{L}'\mathbf{c} - \mathbf{o})^{\mathrm{T}} \mathbf{W} (\mathbf{L}'\mathbf{c} - \mathbf{o}). \quad (12)$$

With this formulation, the analysis is performed in the moving frame to reduce the advection-caused error. This approach is called the advection correction (AC) method.

The AC method neglects the temporal evolution in the moving frame, so the evolution-caused error cannot be reduced effectively. The EC method considers the temporal evolution but in the fixed frame, so the advection-caused error cannot be reduced effectively. Each method has its weakness when it is used individually. Each method has its merit that overcomes the weakness of the other method. When the two methods are properly combined, their merits can be combined effectively to overcome their weaknesses. The combined method is described below.

In the combined method, the time interpolation in (5) is applied to analyze three-dimensional wind fields in the moving frame. In this case, the cost function has the following form:

$$J^o = [T(\mathbf{L}'\mathbf{c}_1, \mathbf{L}'\mathbf{c}_2) - \mathbf{o}]^{\mathrm{T}} \mathbf{W} [T(\mathbf{L}'\mathbf{c}_1, \mathbf{L}'\mathbf{c}_2) - \mathbf{o}]. \quad (13)$$

where the time interpolation operator T is the same as in (7), but in the moving frame. This combined approach is called the evolution–advection correction (EAC) method.

3. Idealized experiments

In this section, three sets of idealized experiments are designed to demonstrate the merits of the EAC method in comparison with the AC and EC methods as well as the NC method in which neither time interpolation nor a moving frame is used. The first set of experiments is to test the sensitivity of the analysis error of each method to the advection of the idealized weather system, the second set is to test the sensitivity to the evolution of the idealized weather system, and the third set is to test the sensitivity of analysis error of each method to the analysis period. The idealized weather system is assumed to be one-dimensional and perfectly sampled by the radar in two successive volume scans. Each volume scan covers a horizontal distance of $D = 80$ km, and the analysis domain is from 0 to D_a (60 km). The time elapsed for one volume scan is τ, the range gate distance is $dx = 1.0$ km, the number of measurement time intervals in each volume scan is $M_1 = M_2 = 80$, and the total number of measurements is $M = M_1 + M_2 + 1 = 161$. The characteristic velocity is $A = 10$ m s^{-1}, the measurements are specified by

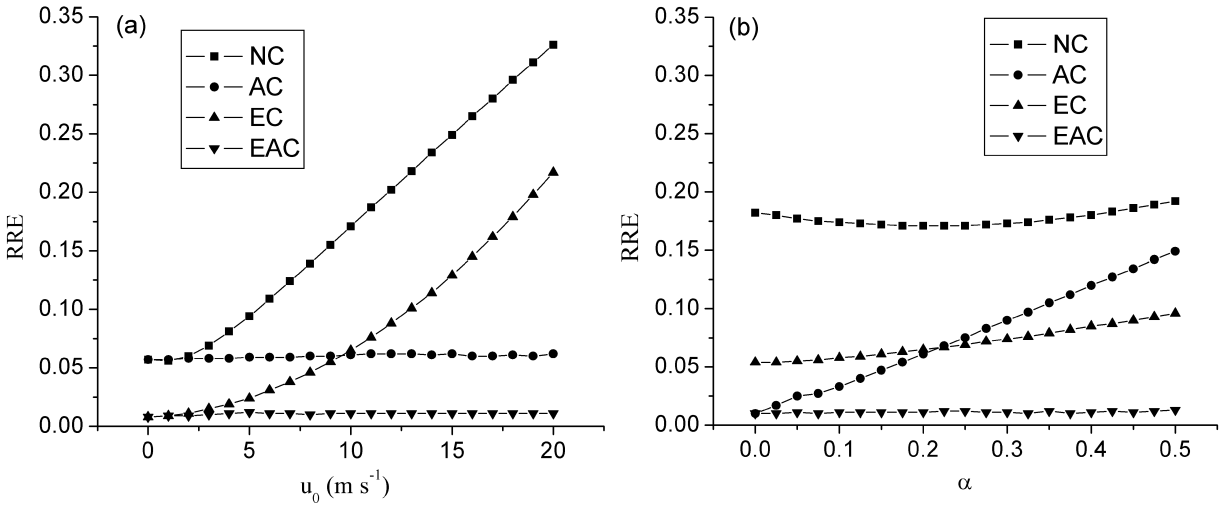

FIG. 1. RREs for the four methods plotted (a) as functions of u_0 with $\alpha = 0.2$ and (b) as functions of α with $u_0 = 10.0$ m s^{-1}.

$$v_r^o(\mathbf{x}_m) = Ae(t_m)s(\mathbf{x}_m, t_m), \tag{14}$$

where $\mathbf{x}_m = (m - 1)dx$ and $t_m = \tau(m - 1)/M_1$, $m = 1, 2, 3, \ldots M_1$ for the first scan, and $\mathbf{x}_m = (m - M_1 - 1)dx$ and $t_m = \tau(m - 1)/M_2$, $m - M_1 = 1, 2, 3, \ldots M_2 + 1$ for the second scan. The variation of the weather system is described by two terms, the evolution term

$$e(t_m) = 1.0 - \alpha\frac{t_m}{2\tau}, \tag{15}$$

and the advection term

$$s(\mathbf{x}_m, t_m) = \sin\left[\frac{2\pi}{D_a}(\mathbf{x}_m - u_0 t_m)\right]. \tag{16}$$

In (14)–(16), the idealized weather system is controlled by three parameters, the evolution coefficient α, the advection speed u_0, and the analysis period (2τ). To evaluate the accuracy of the analysis wind, the relative rms error (RRE) is calculated for each analyzed field by

$$\text{RRE} = \left(\sum |\mathbf{v}^a - \mathbf{v}^t|^2\right)^{1/2}\left(\sum |\mathbf{v}^t|^2\right)^{-1/2}, \tag{17}$$

where $\mathbf{v}^a$ is the analyzed vector wind, $\mathbf{v}^t$ is the true vector wind, and the summation is for all the grid points over the analysis domain. The truncation number of Legendre expansion is set to seven. Three experiments are carried out to test the sensitivity of analysis error to the parameters α, u_0, and τ for each of the aforementioned four methods.

a. Sensitivity to advection

In this first set of experiments α is fixed to 0.2, which means that the intensity of the weather system is reduced by 20% in the entire observation period and τ is fixed to 5 min. The advection speed u_0, however, is set to different values ranging from 0.0 to 20.0 m s^{-1}. Each method is used to analyze the wind field at the beginning time t_1 of the first scan. The RRE is shown for each analysis in Fig. 1a. When the advection speed is smaller than 10 m s^{-1}, the RREs of the EC and EAC methods are less than 7.5%, and it is smaller than the AC method's RRE. Because the temporal evolution dominates the change of the weather system in this case, the AC method cannot reduce the evolution-caused error effectively. This explains why the AC method's RRE is relatively large. When the advection speed becomes larger than 10 m s^{-1}, the RREs of AC and EAC increase only slightly but the EC method's RRE becomes large. Clearly, the EAC method has the best performance with the RRE below 2.5% even as u_0 becomes as large as 20 m s^{-1}. The EC method is more sensitive to the advection speed than the EAC and AC methods.

b. Sensitivity to temporal evolution

In this second set of experiments, the parameter α is set to different values ranging from 0.0 to 0.5, while the advection speed u_0 is fixed to 10.0 m s^{-1} and τ is fixed to 5 min. As in section 3a, each method is used to analyze the wind field at the beginning time t_1 of the first scan. The RRE is shown for each analysis in Fig. 1b. When α is smaller than 0.2, the AC and EAC methods perform better than the other two methods, and their RREs are less than 7.0%. In this case, the local time variation of the weather system is caused mainly by the advection, thus, the AC method becomes more accurate than the EC method, as speculated in the introduction. When α is larger than 0.2, the RREs of the EC and EAC methods increase only slightly, but the AC method's RRE becomes nearly as large as that of NC. As expected, the EAC shows the best performance with RRE below 2.5% over the entire range of α.

c. Sensitivity to analysis period

In this third set of experiments, τ is set to different values ranging from 0 to 10 min, while the advection speed u_0 is fixed to 10.0 m s^{-1} and α is fixed to 0.2. The analysis period for two successive volume scans is 2τ. As in sections 3a and 3b, each method is used to analyze the wind field at the beginning time t_1 of the first scan. The RRE curves (not shown) for the four methods are very similar to those in Fig. 1a except that the horizontal axis is for τ. Again, the EAC performs best while the NC performs worst for the entire range of $0 \leq \tau \leq 10$ min. The EC performs better than the AC method when $0 \leq \tau \leq 5$ min, and the situation reverses when $\tau \geq 5$ min.

As explained in appendix B, the validity or accuracy of the linear evolution assumption relies on the smallness of the analysis period scaled by the decorrelation time scale of the concerned features. As shown by the above idealized experiments, in the ground-fixed frame, the spatial correlation between the wind fields at the beginning and end of the analysis period decreases as the analysis period 2τ becomes large and/or the system advection speed u_0 increases. In the moving frame that follows the system exactly, however, the spatial correlation between the wind fields at the beginning and end of the analysis period is maximized (to 1). This is possible only in the idealized situation, but it implies that using a system-following moving frame can enhance the decorrelation time scale and thus improve the accuracy of the linear time interpolation. The more closely the storm system follows the moving frame, the more accurate the linear time interpolation is in the moving frame. This explains why the EAC method performs best not only for the idealized data in this section but also, as shown in the next two sections, for the simulated data and real radar data.

4. Experiments with simulated radar data

a. Simulated radar data

The Advanced Regional Prediction System (ARPS; Xue et al. 1995) is employed to generate simulated radar data for an extensively studied supercell storm—the Del City storm on 20 May 1977 in Oklahoma. A detailed description of the storm development can be found in Mewes and Shapiro (2002). The model domain size is 64 km $\times$ 64 km $\times$ 15 km. The grid interval is 1.0 km in the horizontal and 0.5 km in the vertical directions. The storm is initiated by a thermal bubble from the sounding centered at $x = 48$ km, $y = 16$ km, and $z = 1.5$ km, while the coordinate origin is at the lower-front-left corner of the grid. The advection speed ($u_0 = 3.0$ m s^{-1} and $v_0 = 14.0$ m s^{-1}) is subtracted from the sounding to keep the simulation as stationary as possible. The integration time step in this simulation is 6 s, and the wind fields relative to the ground are saved every 30 s. These wind fields in the ground-relative frame will be applied to produce simulated radar data to test the four methods.

The simulation shows that the thermal bubble grows into a loosely organized convective cell at $t = 1200$ s and then evolves gradually into a well-organized multicell system. Simulated radar data are generated from $t = 1200$ to 7200 s (the end of the simulation period). The analysis domain covers only the primary supercell storm, which is limited to a volume of 20 km $\times$ 20 km $\times$ 15 km within the model domain. Simulated data are generated for two radars over each analysis period (10 min covering two successive volume scans), and there are a total of 10 analysis periods from $t = 1200$ to 7200 s. During these analysis periods, the simulated storm is not absolutely stationary in the moving frame (with $u_0 = 3.0$ m s^{-1} and $v_0 = 14.0$ m s^{-1}). Sometimes the supercell can shift as much as 2 km in 10 min, and so the moving-frame speed is only an approximation of the mean flow advection. A vertical cross section of the simulated wind field relative to the ground is shown in Fig. 2a at $t = 5400$ s and $y = 10$ km, where the coordinate origin is at the lower-left corner of the analysis domain. As shown, the main updraft is quite strong, but the downdraft near the right-lower corner is weak and not yet fully developed at this time, indicating that the supercell is nearly but not yet matured.

In the previous studies of Gao et al. (1999) and Mewes and Shapiro (2002), when the simulated radar data were generated, the mean flow advection was simply neglected. Thus, implicitly, it was assumed that the radars were moving with the storm during the entire observation period, and this was an unrealistic situation for ground-based radars. In this paper, the averaged storm motion relative to the ground has been taken into consideration. In particular, the two radars are ground fixed at (10, 40, 0.0) and (40, 10, 0.0) km, respectively, where the coordinate origin is at the lower-left corner of the analysis domain at the initial time for each analysis period. To mimic the Next Generation Weather Radar (NEXRAD) severe storm radar-scanning mode, each simulated radar volume scan consists of 14 elevations from 0.5° to 20°, with an azimuthal resolution of 1° and range gate interval of 250 m. Each volume scan is completed in 5 min with each beam position determined and timed accurately for the simulated radar observations. A total of 20 radar volume scans are generated.

b. Wind analyses

By using the above simulated radar data, wind analyses are performed for all 10 analysis periods by the four (NC, AC, EC, and EAC) methods. Only the AC and EAC methods require consideration of the advection speed ($u_0 = 3$ m s^{-1}, $v_0 = 14$ m s^{-1}) for the fast-moving supercell. The remaining parameter settings for the four methods are given as follows: The truncation number of the Legendre expansion is set to seven in each direction. The weights for the observation term, continuity

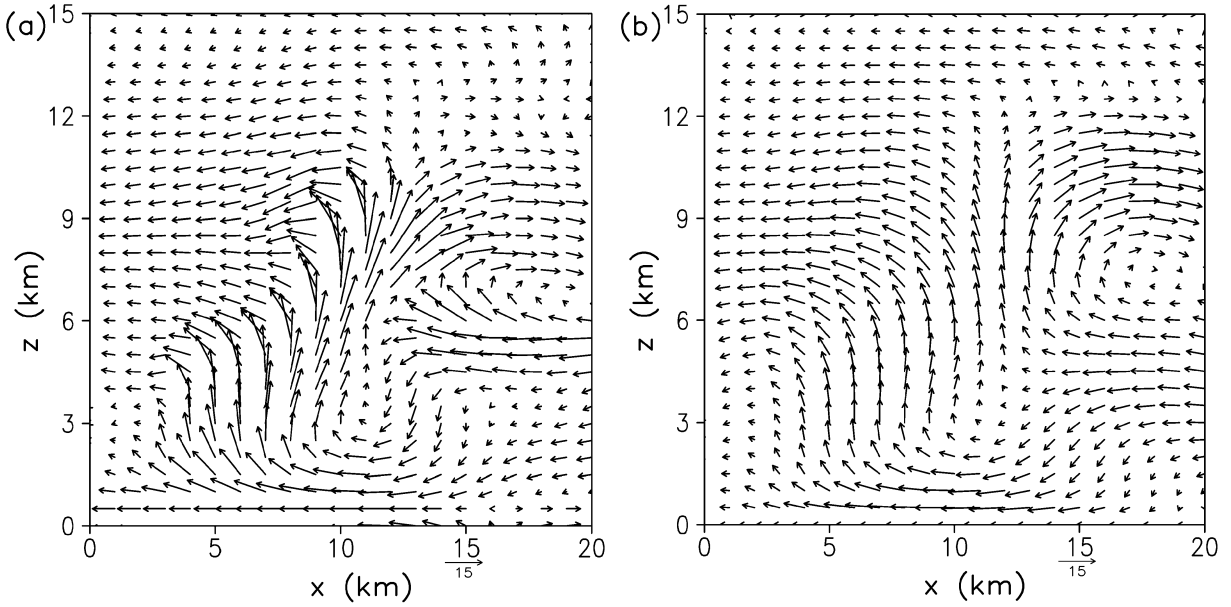

FIG. 2. (a) Simulated wind field and (b) EAC-analyzed wind field in the vertical cross section at $y = 10.0$ km.

equation and boundary constraints are 1.0 (m^{-2} s^2), 1.0 $\times$ 10^5 (s^2), and 1.0 $\times$ 10^{-1} (m^{-2} s^2), respectively. These values depend on the error statistics of their associated terms. They are chosen empirically in this paper to ensure that the constraints have proper orders of magnitude.

The performances of the four methods can be evaluated by the rms, RRE, and correlation coefficient [CC; as defined in (4) of Xu et al. 2001] of the analyzed three-dimensional vector wind fields with respect to the model that is simulated. The time sequences of CC and RRE are plotted in Figs. 3a and 3b for the 10 consecutive analysis periods. The sequence of rms (not shown) has a similar pattern as that of RRE in Fig. 3b. Their average values over the 10 analysis periods are listed in Table 1. Among the four methods, the NC method performs worst because it has the largest average RRE and lowest average CC (only 0.64). The average CC for the EC method is about 3% higher than that for the NC method (see Table 1), but the average rms for the EC method is slightly larger than that for the NC method. The RRE in Fig. 3b also shows that the EC method performs slightly worse than the NC method for three analysis periods (i.e., the 5th, 6th, and 7th periods between t = 3000 s and t = 5400 s). During these three analysis periods, the simulated supercell develops very rapidly. When the supercell evolution is reviewed in the fixed frame for these three analysis periods, the wind time variation becomes highly nonlinear. In this case, the linear evolution assumption in the EC method could

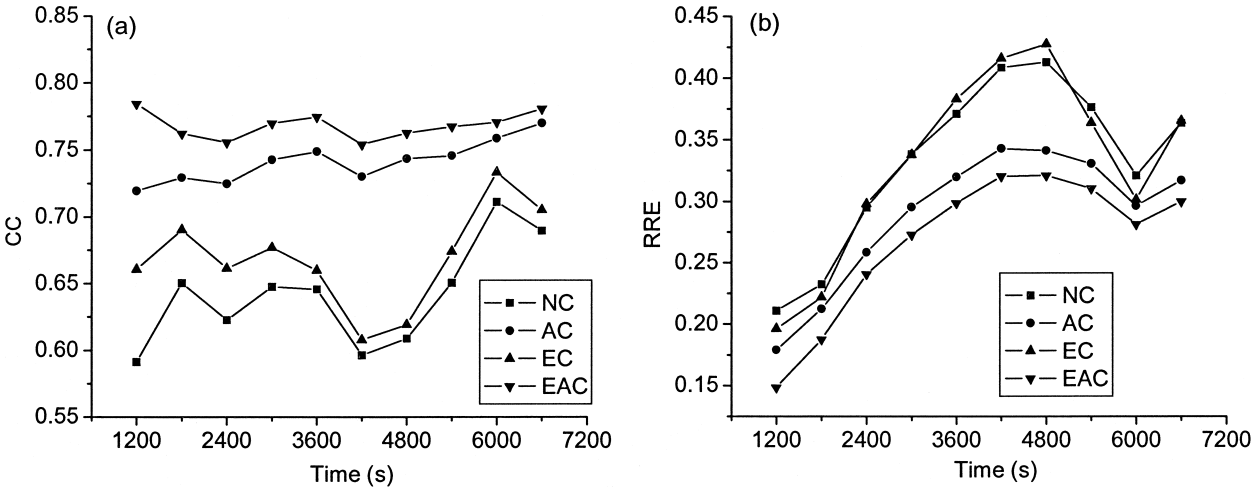

FIG. 3. Plots of (a) CCs and (b) RREs for the four methods over the 10 analysis periods.

TABLE 1. Averaged CC, rms (m s^{-1}), and RREs over the 10 analysis periods for the four methods.

Method	CC	RRE	Rms
EAC	0.768	0.264	2.548
EC	0.670	0.331	3.143
AC	0.731	0.296	2.853
NC	0.642	0.334	3.138

become very inaccurate. This may explain why the EC method performs worse than the NC method for the above three analysis periods.

The results in Table 1 show that the AC and EAC methods perform better than the other two methods. Clearly, using the moving frame is effective in improving the analysis for such a fast-moving supercell. In particular, the average RRE for the AC method shows a nearly 4% reduction compared to the NC method. When the evolution correction is implemented by the EAC method in combination with the advection correction, the average RRE is further reduced by 3%, so there is a total 7% reduction in the averaged RRE for the EAC method in comparison with the NC method. The effectiveness of the combination of the evolution and advection corrections is also seen from the results in Figs. 3a and 3b. For all the 10 analysis periods, the EAC method analyses have the smallest RRE (Fig. 3b) and have the largest CC (Fig. 3a). The EAC method is clearly the best. An example of the EAC-analyzed wind field relative to ground is shown in Fig. 2b. As shown, the analyzed wind field has captured all the major structures in the simulated ''true'' wind field (Fig. 2a), although the analyzed wind field is relatively smooth (because small-scale structures are filtered by the Legendre polynomial expansion).

c. Sensitivity to uncertainty in the moving-frame speed

The above experiments demonstrate that the EAC method performs better than the other three methods for the simulated fast-moving supercell. Additional experiments are performed for simulated supercells with different advection speeds. The results (not shown) indicate that the improvement of the EAC method over the EC and NC methods becomes more (or less) significant if the supercell advection speed becomes faster (or slower). This is consistent with the idealized experiments in section 3. However, unlike the idealized experiments, the simulated supercell is not exactly stationary in the selected moving frame. As mentioned in section 4a, sometimes the supercell can shift as much as about 2 km in 10 min. This implies that the advection speed of the supercell has an uncertainty in the range of $\pm 20\%$, and so does the selected speed for the moving frame. Thus, it is necessary to examine the sensitivity of the EAC method with respect to uncertainty in the advection speed.

TABLE 2. Averaged RREs for different perturbations (percentages) to the moving frame speed.

Percentage (%)	−20	−10	0	10	20
RRE	0.289	0.268	0.264	0.269	0.280

Sensitivity experiments are performed with the moving-frame speed perturbed by $\pm 10\%$ and $\pm 20\%$, respectively, around $(u_0, v_0) = (3, 14)$ m s^{-1}. The average RRE for the EAC method analyses over the 10 analysis periods are listed in Table 2 for the above perturbed percentages of the moving-frame speed. As shown, the RRE increases slowly as the moving-frame speed is perturbed increasingly away from $(u_0, v_0) = (3, 14)$ m s^{-1}. In particular, the RRE of the EAC method analyses is increased only slightly, no more than 4%, to 0.28 (or 0.29) even when the moving-frame speed is perturbed by $+20\%$ (or -20%). These increased RREs are still smaller than the RRE of the NC method analyses (which is 0.33 as listed in Table 1). It is also notable that the RRE is increased less than 1% when the moving-frame speed is perturbed by $\pm 10\%$. Thus, the EAC method is not very sensitive to uncertainty in the moving-frame speed.

d. Validity of the linear evolution assumption

As explained in the introduction section, the EAC method assumes implicitly that the time evolution of the storm is nearly linear in the moving frame during two successive volume scans (10 min). Because the improvement of the EAC method over the AC and NC methods may depend on this assumption, it is necessary to examine the validity or accuracy of this linear evolution assumption in the moving frame. The time evolution of the three-dimensional wind fields associated with a supercell storm is essentially nonlinear regardless of whichever frame is used. The validity and accuracy of the above linear evolution assumption can be quantified by the RRE between the simulated vector winds and the linearly interpolated winds (obtained from the two simulated wind fields at the beginning and ending times) over each analysis period. Ten RRE values are calculated for the 10 analysis periods and their averaged value is only 0.087 (see Table 3). Thus, the above linear evolution assumption should be valid at least for the simulated supercell over each 10-min analysis period in the moving frame.

As explained in the idealized experiments, the accuracy of the above linear evolution assumption is ex-

TABLE 3. RREs for different time lengths of the analysis period.

	5 min	10 min	15 min	20 min
Moving frame	0.034	0.087	0.133	0.168
Fixed frame	0.145	0.252	0.283	0.292

pected to increase (or decrease) when the analysis period decreases (or increases). This is further verified by the results listed in Table 3. As shown, the averaged RRE decreases rapidly from 0.168 to 0.034 when the analysis period decreases from 20 to 5 min. When the linear evolution assumption is applied to the ground-fixed frame, all the averaged RREs are increased several times. In this case, as shown by the second row in Table 3, the averaged RREs exhibit the similar dependence on the analysis period, but at a much higher level than those in the first row for the moving-frame case.

The validity and accuracy of the linear evolution assumption are further examined theoretically in terms of optimal interpolation based on Bayesian probability estimation theory in appendix B, where the intrinsic merit of using a moving frame to improve radar wind analyses is explained physically. As explained in appendix B, the accuracy of the linear interpolation depends on the smallness of the analysis period scaled by the decorrelation time scale of the concerned features. Using a moving frame can increase the decorrelation time scale, so this time scale can become sufficiently larger than the analysis period ($\leq$10 min) in a moving frame. This explains why the linear time interpolation can be more accurate in a moving frame than in a ground-fixed frame.

e. The effects of data coverage and analysis resolution

As explained in section 4a, each simulated radar volume scan consists of 14 elevation angles (0.5°, 1.5°, 2.5°, 3.5°, 4.5°, 5.5°, 6.2°, 7.5°, 8.7°, 9.9°, 12.0°, 14.6°, 16.7°, 19.5°), which are exactly the same as those used in the NEXRAD severe storm radar-scanning mode. Because of this, the data resolution and coverage decrease with height quite rapidly. Besides, because the simulated storm is close to the two radars, the top portion of the storm near the upper boundary of the analysis domain is partially above the top-elevation scan (19.5° from each radar). This causes a data-void region near the upper boundary of the analysis domain (and the situation is slightly worse than that in the real data experiment discussed in the next section). Similarly, there is another data-void region immediately above the surface boundary underneath the lowest scan (0.5° from each radar). In these data-void regions, observations are actually extrapolated. Thus, it is necessary to examine the effectiveness of the involved extrapolation and related errors. For this purpose, the average RREs and CCs over the 10 analysis periods are computed for each of the 30 vertical levels (used in the analysis). The results are plotted in Fig. 4. As shown, the RRE jumps and the CC drops sharply at the lowest two vertical levels, so the extrapolation is not very effective in the data-void region immediately above the lower boundary. Toward the top boundary (at $z = 15$ km), the RRE decreases and the CC increases gradually, and so the overall quality of the analysis does not change much in the data-void region near the upper boundary. Note that the wind field is relatively strong and has a sharp gradient near the lower boundary but becomes relatively weak and smooth near the upper boundary, and so the extrapolation should be more effective in the data-void region near the upper boundary than near the lower boundary. This explains the above-described results in Fig. 4. Apparently, the accuracy of the analysis in a data-void region could be affected not only by the size of data-void region but also by the intensity and complexity of the wind field therein.

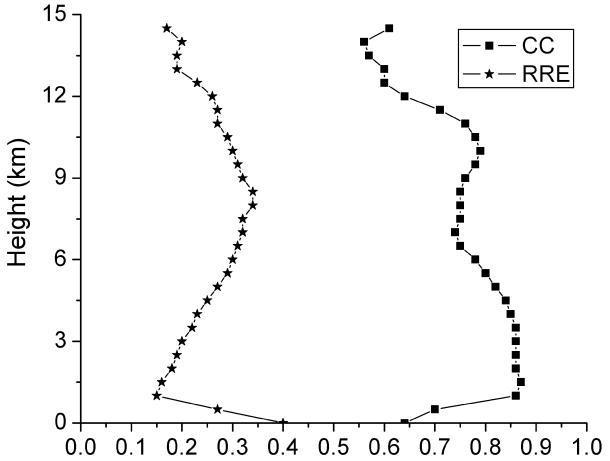

FIG. 4. Averaged RREs and CCs plotted as function of height.

The order of the Legendre polynomial expansion used in the EAC method is another factor that can influence the analysis directly in both data-rich and data-void regions. Thus, additional experiments are performed to test the sensitivity of analysis error to the expansion order over a wide range (from 3 to 9). Each expansion order is applied with the EAC method to retrieve the wind field at $t = 5400$ s. The results show continuous improvements in the accuracies of the retrievals as the order increases, but the improvements became insignificant as the order became larger than 7. In view of the increased computational cost, the expansion order to 7 is selected for the storm wind analysis in this paper. However, to apply the method to further-refined convective or smaller-scales phenomena, the expansion order may need to be increased unless the analysis domain is reduced.

In this section, numerical experiments have been performed with simulated radar data. The results are consistent with those obtained from the idealized experiments in section 3. In addition, when tested with the simulated radar data, the EAC method is found to be rather robust to uncertainty in the moving-frame speed. The linear evolution assumption used by the EAC method in the moving frame is also found to be acceptable for the selected analysis period ($\leq$10 min). The effects of data coverage and analysis resolution (determined by the expansion order) are also examined in the connec-

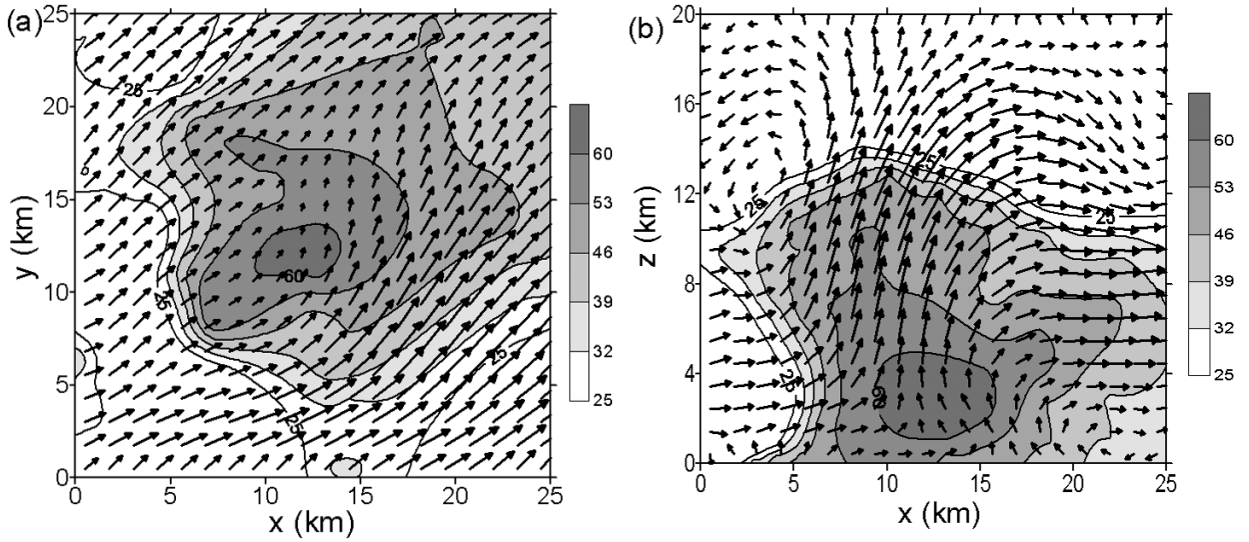

FIG. 5. Reflectivity (shaded) and EAC-analyzed vector winds at 1632 CST in (a) the horizontal cross section at $z = 4.0$ km and (b) in the vertical cross section at $y = 12.5$ km.

tion with real data applications. In the next section, the EAC method will be further tested with real Doppler velocity data in comparison with the other three methods.

5. Real-case experiments

In this section, the four methods compared in previous section are applied to a real case of supercell storm. This storm was observed by the Norman radar and Cimarron radar as it occurred on 17 May 1981 at Arcadia, Oklahoma. The distance between the two radars is about 50 km. The storm was in a pretornadic stage. More detailed descriptions about the storm can be found in Dowell and Bluestein (1997). Two volume scans from each radar at 1632 and 1636 central standard time (CST) are used in the analysis. Each volume scan takes about 4 min and consists of 14 elevation angles (from 0.5° to 23.2° for the Norman radar and from 0.7° to 34.16° for the Cimarron radar). Thus, data coverage near the upper boundary is slightly better than that considered in the simulated radar data experiments. The analysis domain is 25 km × 25 km × 20 km. The origin (0, 0, 0) is set at the lower-left corner of the analysis domain, with the Cimarron radar located at (−13.0, 1.0, −0.43) and the Norman radar at (18.80, −25.60, 0.0). The horizontal (at $z = 4.0$ km) and vertical (at $y = 12.5$ km) cross sections of reflectivity (shaded) at 1632 CST from the Cimarron radar are shown in Figs. 5a–b. In Fig. 5a, the maximum reflectivity is above 60 dBZ at the center of analysis domain. The vertical cross section is plotted through the maximum reflectivity point in Fig. 5b. In this vertical cross section, the maximum reflectivity is at about $z = 2.5$ km.

To estimate the advection speed, the radar-observed reflectivity fields at 1632 and 1636 CST are interpolated to a Cartesian grid with $\Delta x = \Delta y = 500$ m and $\Delta z = 400$ m. These spatial interpolations are performed by the Barnes scheme with two iterations (Daley 1991). The influence radii are set to $6\Delta x$ in the horizontal and $6\Delta z$ in the vertical for the first iteration, and are then reduced by 3 times for the second iteration. The advection velocity is estimated from the movement of the main reflectivity pattern (>30 dBZ) by using (10)–(11) of Gal-Chen (1982). The estimated vector velocity is $(u_0, v_0) = (6.0, 12.0)$ m s^{-1}, indicating that the supercell was propagating at the speed of 13.4 m s^{-1} north-northeastward. During the period of the two volume scans (8 min), the supercell moved 6.4 km. The weights and the truncation number of Legendre expansion are the same as in the simulated radar observations experiments. The four methods are applied to these two volume scans, and the analyzed wind fields are compared at the single time level of 1632 CST.

Shown in Figs. 5a and 5b are the horizontal cross section at $z = 4.0$ km and the vertical cross section at $y = 12.5$ km, respectively, of the three-dimensional wind field analyzed by the EAC method. Figure 5a shows that the convergence center of the analyzed wind coincides with the maximum reflectivity center. Figure 5b shows that the vertical circulation is characterized by four major components: (i) an inflow from the left side in the lower and middle troposphere, (ii) an updraft within the main storm tower that overshoots beyond the tropopause, (iii) a strong divergent flow near and above the tropopause, and (iv) a major branch of outflow to the right side in the middle and upper troposphere. The maximum vertical velocity in the updraft core reaches 37 m s^{-1}, while the updraft core is on the upstream side about 5 km ahead of, and 6–8 km above, the reflectivity core in Fig. 5b. The analyzed wind field captures all of

TABLE 4. CCs, rms (m s^{-1}), and RRDs for AC, EC, and NC vs EAC benchmark.

	u			*v*			*w*		
Method	CC	RRE	Rms	CC	RRE	Rms	CC	RRE	Rms
NC	0.937	0.247	4.124	0.932	0.249	3.826	0.922	0.348	3.501
AC	0.962	0.192	3.196	0.971	0.147	2.263	0.970	0.218	2.198
EC	0.965	0.184	3.064	0.968	0.162	2.486	0.957	0.251	2.524

the major features in the conceptual model of supercell storms (see Chapter 9 of Doviak and Zrnic 1993).

Because the true wind field is not known, the wind field obtained by the EAC method is used as a benchmark, a proxy of the true wind field, to evaluate the performances of the remaining three methods. The rms, relative rms difference (RRD), and CC are computed for each velocity component field obtained by each method in comparison with that obtained by the EAC method. The results are listed in Table 4. As shown, the NC analysis yields the greatest difference when compared with the benchmark EAC analysis. Because the advection speed is large (13.4 m s^{-1}) and the storm is fully developed into a pretornadic stage, the temporal evolution is relatively slow in the moving frame. Consequently, the difference between AC and EAC methods is smaller than that between the EC and EAC methods in the *w*-component and v-component fields. However, because the *u* component of the advection ($u_0 = 6.0$ m s^{-1}) is only one-half that of the v component ($v_0 = 12.0$ m s^{-1}), the advection-caused error may be relatively small in the *u*-component field. This may explain why the EC method–analyzed *u*-component field is slightly nearer to the EAC–than the AC method–analyzed field. This agrees with the results obtained from the idealized experiments in section 3.

6. Conclusions

To reduce errors caused by the traditional time interpolation in Doppler wind analyses, two methods were previously developed. One was designed to correct the evolution-caused error and is called the EC method (Liu and Qiu 2003), while the other was designed to correct the advection-caused error and is called the AC method (Gal-Chen 1982). It is shown in this paper that the AC and EC methods can be combined into a new (EAC) method. By performing time interpolation in the moving frame in the analysis space, this new method can effectively correct both the evolution-caused and advection-caused errors. The merits of this new method are demonstrated by idealized experiments, simulated radar observation experiments, and real-case experiments, in comparison with the traditional (NC) method as well as the previous EC and AC methods.

The results of the idealized experiments show that the EC method is sensitive to the advection speed and the AC method is sensitive to the temporal evolution, while the EAC method has the smallest error and much-reduced sensitivities. The simulated radar data experiments further demonstrate that the EAC method can significantly improve the wind analyses compared with the other three methods for all of the 10 analysis periods. Besides, the EAC method is found to be not very sensitive to uncertainty in the moving-frame speed. The linear evolution assumption used by the EAC method is also shown to be acceptable in the moving frame, as long as the analysis period is relatively short ($\leq$10 min). The real-case experiments show that the wind field analyzed by the EAC method captures all the major features of the storm. The EAC-analyzed wind field is thus used as a benchmark to evaluate the other three methods. The evaluation results are consistent with the idealized and simulated radar data experiments.

For a disorganized or poorly organized storm system, no single advection speed can be defined. The EAC method developed in this paper is thus not suitable for such a system. However, if an individual storm is well organized within a scattered or multicell storm system, then the EAC method should be able to be applied to this individual storm (rather than the entire system). Under this limitation, the EAC method has a merit in improving radar wind analyses. In this paper, the improved time interpolation is implemented with the EAC method for dual-Doppler wind analyses only. This technique may be also implemented with other least squares methods, such as those used for single-Doppler wind retrievals (Qiu and Xu 1996) and thermodynamic retrievals, to reduce the advection-caused errors and evolution-caused errors. Further investigations are needed in this direction.

Acknowledgments. The authors are thankful to Dr. Jidong Gao at the Center for Analysis and Prediction of Storms for providing the Doppler radar data and to the anonymous reviewers for their comments and suggestions that improved the presentation of the results. This research was supported by the NSF Grant ATM-9983077, ONR Grants N000140310822 and N000140410312, and by the National Science Foundation of China (40175010).

APPENDIX A

MANDOP Method

As with the MANDOP (Scialom and Lemaître 1990), each component of the analyzed vector wind field is

expressed by a three-dimensional expansion of Legendre polynomial in the Cartesian coordinates over the analysis domain. In particular, the ith wind component ($i = 1, 2, 3$) is expressed by

$$v_i = \sum_{k_i=1}^{N_i} c_{k_i} g_{k_i}(\mathbf{x}), \tag{A1}$$

where c_{k_i} is the kth expansion coefficient, g_{k_i} is the kth basis function composed of three one-dimensional Legendre polynomials, each in one of the three spatial dimensions, and N_i is the truncation number of the expansion. The basis functions g_{k_i} ($k = 1, 2, \ldots N_i$) are orthonormal in the L_2 space. The radial wind field is then given by

$$v_r^a(\mathbf{x}) = \sum_{i=1}^{3} d_i v_i = \sum_{i=1}^{3} d_i \sum_{k_i=1}^{N_i} c_{k_i} g_{k_i}(\mathbf{x}), \tag{A2}$$

where $(d_1, d_2, d_3) = [(x - x_r)/r_d, (y - y_r)/r_d, (z - z_r)/r_d]$ are direction cosines, $r_d = [(x - x_r)^2 + (y - y_r)^2 + (z - z_r)^2]^{1/2}$ is the radial distance from radar, and (x_r, y_r, z_r) are radar positions in the analysis domain. Rearranging (A2) leads to the following form:

$$v_r^a(\mathbf{x}) = \sum_{K=1}^{N} c_K L_K(\mathbf{x}), \tag{A3}$$

where $N = N_1 + N_2 + N_3$,

$$K = \begin{cases} k_i & \text{for } i = 1, \\ N_1 + k_i & \text{for } i = 2, \\ N_1 + N_2 + k_i & \text{for } i = 3, \end{cases} \quad \text{and}$$

$$L_K(\mathbf{x}) = d_i g_{k_i}(\mathbf{x}). \tag{A4}$$

The projection of the analyzed radial wind field in the observation space is a vector defined by

$$\mathbf{a} = [v_r^a(\mathbf{x}_m) \,|\, m = 1, 2, \ldots M]. \tag{A5}$$

Substituting (A3) into (A5) gives

$$\mathbf{a} = \mathbf{L}\mathbf{c}, \tag{A6}$$

$$\mathbf{L} = \begin{bmatrix} L_1(\mathbf{x}_1) & L_2(\mathbf{x}_1) & \cdots & L_N(\mathbf{x}_1) \\ L_1(\mathbf{x}_2) & L_2(\mathbf{x}_2) & \cdots & L_N(\mathbf{x}_2) \\ \cdots & \cdots & \cdots & \cdots \\ L_1(\mathbf{x}_M) & \cdots & \cdots & L_N(\mathbf{x}_M) \end{bmatrix}, \qquad \mathbf{c} = \begin{pmatrix} c_1 \\ \cdots \\ \cdots \\ \cdots \\ c_N \end{pmatrix}, \tag{A7}$$

where the elements of matrix $\mathbf{L}$ are determined by the position of the measurements and truncation number N. The elements of vector $\mathbf{c}$ are the coefficients of the basis functions. The observation vector can be denoted by $\mathbf{o} = [v_r^{\text{obs}}(\mathbf{x}_m) \,|\, m = 1, 2, \ldots M]$ where M is the total number of measurements. The observation term in the cost function then has the following form:

$$J^o = (\mathbf{L}\mathbf{c} - \mathbf{o})^{\mathrm{T}} \mathbf{W} (\mathbf{L}\mathbf{c} - \mathbf{o}), \tag{A8}$$

where $\mathbf{W}$ is a $M \times M$ weight matrix in general. Because the measurement errors are assumed to be unbiased and noncorrelated in this paper, $\mathbf{W}$ has a diagonal form. Weak constraints of the continuity equation and boundary conditions are also included in the cost function in this paper. The details are given in Liu and Qiu (2003).

APPENDIX B

Validity of Linear Time Interpolation

The validity of the linear evolution approximation and the possible errors caused by the linear time interpolation can be examined based on Bayesian probabilistic estimation theory. When the background and observation errors are assumed to be Gaussian random and independent of each other, the Bayesian probabilistic estimation theory leads to the conventional variational formulation that yields the statistically optimal interpolation [see chapter 4 of Daley (1991) or chapter 5 of Jazwinski (1970)]. According to Xu et al. (2003), the radar wind observation (measurement and sampling) errors are not correlated beyond adjacent beams (separated in time by a time scale much shorter than a second for the conventional radar scans). Thus, the radar wind observation errors are not correlated in time between two consecutive volume scans (separated by at least 5 min). The background errors, however, are correlated in time. Because the radar wind analyses are performed with zero background wind in this paper, the background errors are simply the true winds and the background error covariance is the covariance of the true wind perturbations.

Under the above conditions, the representer method (see section 4b of Xu and Gong 2003) can be readily applied to the statistical interpolation considered here in the time dimension. In this case, the optimal (maximum likelihood) estimate of the true field has the following time-continuous form:

$$a(t) = \sum_i z_i C(t - t_i), \tag{B1}$$

where Σ_i denotes the summation over $i(=1, 2)$, z_i is the coefficient to be determined for $C(t - t_i)$, t_i is the ith observation time, and $C(t)$ denotes the correlation function for the background errors. As an intermediate state vector $\mathbf{z} = (z_1, z_2)$ is determined by

$$(\mathbf{C} + \mathbf{I}r)\mathbf{z} = \mathbf{d}, \tag{B2}$$

where $\mathbf{C}$ is the background error correlation matrix with its ijth element given by $C_{ij} = C(t_j - t_i)$, $\mathbf{I}$ is the identity matrix in the observation space, $r = \sigma_o^2/\sigma_b^2$ is the ratio between the observation error variance σ_o^2 and background error variance σ_b^2, and $\mathbf{d}$ is the observation innovation vector. Because a zero background field is used, the ith component of $\mathbf{d}$ is simply the observation at t_i. As explained earlier, the observation errors at the two observational times (t_1 and t_2) are not correlated, and so the observation error covariance matrix is di-

agonal and is given by $\sigma_o^2\mathbf{I}$. The derivation of (B1)–(B2) is similar to that of (4.8)–(4.9) in Xu and Gong (2003), except that the continuous functions are considered in the temporal instead of the spatial dimension.

The interpolation function $a(t)$ obtained from (B1)–(B2) is statistically optimal. This optimal interpolation function can be close to linear if the correlation function $C(t)$ is close to linear on each side of $t = 0$ within the range of the analysis time window $\tau = t_2 - t_1$. As an extreme example, the correlation function may be roughly approximated by the following simple triangle shape:

$$C(t) = 1 - \min(1, |t|/\tau_0), \tag{B3}$$

where τ_0 (>0) is the zero-correlation time scale. Denoted by $a(t) = a_{\text{lin}}(t)$ is the solution of (B1)–(B3). It is easy to see that $a_{\text{lin}}(t)$ is a linear function between $t_1 \le t \le t_2$ as long as $\tau_0 \ge \tau$. According to (B2), the two components of $\mathbf{z} = (\mathbf{C} + \mathbf{I}r)^{-1}\mathbf{d}$ have the following general forms:

$$z_1 = \frac{pd_1 - qd_2}{p^2 - q^2} \quad \text{and} \quad z_2 = \frac{pd_2 - qd_1}{p^2 - q^2}, \tag{B4}$$

where $p = 1 + r$ and $q = \max(0, \boldsymbol{\tau}_0 - \boldsymbol{\tau})/\boldsymbol{\tau}_0$ are the diagonal and off-diagonal elements of $\mathbf{C} + \mathbf{I}r$, respectively. Substituting (B3)–(B4) into (B1) gives

$$a_{\text{lin}}(t) = a_{\text{lin1}}(t) + a_{\text{lin2}}(t), \tag{B5a}$$

$$a_{\text{lin1}}(t) = d_0(1 + q)/(p + q), \quad \text{and} \tag{B5b}$$

$$a_{\text{lin2}}(t) = \Delta d(2\Delta t/\tau - \tau/\tau_0)/(p - q), \tag{B5c}$$

where $d_0 = (d_1 + d_2)/2$, $\Delta d = (d_2 - d_1)/2$, $\Delta t = t - t_1$, $\tau_0 \ge \tau$, and, thus, $q = 1 - \tau/\tau_0 = 0$ are assumed. In the limit of $r \to 0$ (and, thus, $p \to 1$), $a_{\text{lin}}(t)$ passes through the two observations, that is, $a_{\text{lin}}(t_i) = d_i (i = 1, 2)$. In this case, the results in (B5) become independent of τ_0 (with $\tau_0 \ge \tau$), and $a_{\text{lin}}(t)$ is just the linear time interpolation used in this paper.

The true correlation function is likely to have the following Gaussian shape [instead of the triangle shape in (B3)]:

$$C(t) = \exp(-t^2/\tau_d^2), \tag{B6}$$

where τ_d is the decorrelation time scale defined by $\tau_d = -2C(d^2C/dt^2)^{-1}$. The solution of (B1)–(B2) with (B6), denoted by $a_{\text{opt}}(t)$, is thus likely to be the true optimal interpolation. In this case, the two components of $\mathbf{z}$ have the same forms as those in (B4) except that $q = \exp(-\tau^2/\tau_d^2)$ according to (B6). Substituting these components with (B6) into (B1) gives

$$a_{\text{opt}}(t) = a_{\text{opt1}}(t) + a_{\text{opt2}}(t),$$

$$a_{\text{opt1}}(t) = d_0\frac{\exp(-\Delta t^2/\tau_d^2) + \exp[-(\Delta t - \tau)^2/\tau_d^2]}{p + q}, \tag{B7a}$$

and (B7b)

$$a_{\text{opt2}}(t) = \Delta d\frac{\exp[-(\Delta t - \tau)^2/\tau_d^2] - \exp(-\Delta t^2/\tau_d^2)}{p - q}, \tag{B7c}$$

TABLE B1. RRDs for different values of τ/τ_d.

τ/τ_d	1	2	3	4
Opt1	0.139	0.056	0.027	0.015
Opt2	0.086	0.024	0.011	0.006
Opt1 + Opt2	0.223	0.080	0.038	0.021

where $q = \exp(-\tau^2/\tau_d^2)$. As expected, $a_{\text{opt}}(t)$ also passes through the two observations in the limit of $r \to 0$.

Now we can show that the linear interpolation $a_{\text{lin}}(t)$ in (B5) (with $\tau_0 \ge \tau$) can be a good approximation of the optimal interpolation $a_{\text{opt}}(t)$ in (B7) as long as τ_d/τ is sufficiently large. Because $|a_{\text{lin}}(t) - a_{\text{opt}}(t)|$ increases slowly as $r \to 0$ (with all other parameters fixed), we only need to examine the difference between $a_{\text{lin}}(t)$ and $a_{\text{opt}}(t)$ for the case of $r = 0$ (and thus $p = 1$). In this case, $|a_{\text{lin1}}(t) - a_{\text{opt1}}(t)|$ is zero at $t = t_i (i = 1, 2)$ and reaches the maximum value of $d_0[1 - 2q^{1/4}/(1 + q)]$ at $\Delta t = \tau/2$ where $q = \exp(-\tau^2/\tau_d^2)$, while $|a_{\text{lin2}}(t) - a_{\text{opt2}}(t)|$ is also zero at $t = t_i (i = 1, 2)$; but, it reaches the maximum at $\Delta t/\tau = \lambda$ where λ is the solution of $(1 - \lambda)\exp[-(1 - \lambda)^2\tau^2/\tau_d^2] - \lambda\exp(-\lambda^2\tau^2/\tau_d^2) = (1 - q)\tau_d^2/\tau^2$. Note that $\max(|d_1|, |d_2|) \ge \max(|d_0|, |\Delta d|)$, so that

$$\frac{|a_{\text{lin}}(t) - a_{\text{opt}}(t)|}{\max(|d_1|, |d_2|)} \le \frac{|a_{\text{lin1}}(t) - a_{\text{opt1}}(t)|}{|d_0|} + \frac{|a_{\text{lin2}}(t) - a_{\text{opt2}}(t)|}{|\Delta d|}. \tag{B8}$$

The maxima for the two terms on the right-hand side of (B8) are functions of τ_d/τ only, and the computed maxima are listed in the first two rows of Table B1. Their sum estimates the upper bound for the term on the left-hand side of (B8), that is, the difference between the linear interpolation and the optimal interpolation scaled by $\max(|d_1|, |d_2|)$. As shown by the third row of Table B1, the estimated upper bound decreases rapidly as τ_d/τ increases. When τ_d/τ increases to 2.0, the scaled difference is bounded by 0.08. In this case, the linear interpolation is very close to the optimal interpolation and the relative difference is smaller than 8%.

As explained earlier, because zero background is used, the background errors are the true winds. For a fast-moving supercell storm, the true winds (for the scales resolved by the model simulations presented in this paper) should be well correlated in time for a substantially longer period in a storm following moving frame than in a ground-fixed frame. Consequently, the decorrelation time scale τ_d can be sufficiently larger than the analysis period τ ($\le$10 min) in the moving frame. This explains physically why the linear time interpolation can be used in the moving frame. This physical interpretation is supported not only by the theoretical results in Table B1, but also by the numerical results in Table 3. Although the true correlation function is assumed to have a Gaussian shape in (B6), this assumption

is not essential. As long as the true correlation function is smooth and has a sufficiently large decorrelation time scale defined by $\tau_d = -2C(d^2C/dt^2)^{-1}$, the qualitative aspect of the results in Table B1 should remain the same.

REFERENCE

Caillault, K., and Y. Lemaître, 1999: Retrieval of three-dimensional wind fields corrected for the time-induced advection problem. *J. Atmos. Oceanic Technol.,* **16,** 708–722.

Chong, M., J. Testud, and F. Roux, 1983: Three-dimensional wind field analysis from dual-Doppler radar data. Part II: Minimizing the error due to temporal variation. *J. Climate Appl. Meteor.,* **22,** 1216–1226.

Clark, T. L., F. I. Harris, and C. G. Mohr, 1980: Errors in wind fields derived from multiple-Doppler radars: Random errors and temporal errors associated with advection and evolution. *J. Appl. Meteor.,* **19,** 1273–1284.

Daley, R., 1991: *Atmospheric Data Analysis.* Cambridge University Press, 457 pp.

Doviak, R. J., and D. S. Zrnic, 1993: *Doppler Radar and Weather Observations.* 2d ed. Academic Press, 562 pp.

Dowell, D. C., and H. B. Bluestein, 1997: The Arcadia, Oklahoma, storm of 17 May 1981: Analysis of a supercell during tornadogenesis. *Mon. Wea. Rev.,* **125,** 2562–2582.

Gal-Chen, T., 1982: Errors in fixed and moving frame of references: Applications for conventional and Doppler radar analysis. *J. Atmos. Sci.,* **39,** 2279–2300.

Gao, J., M. Xue, A. Shapiro, and K. K. Droegemeier, 1999: A variational method for the analysis of three-dimensional wind fields from two Doppler radars. *Mon. Wea. Rev.,* **127,** 2128–2142.

Jazwinski, A. H., 1970: *Stochastic Processes and Filtering Theory.* Academic Press, 376 pp.

Laroche, S., and I. Zawadzki, 1994: A variational analysis method for retrieval of three-dimensional wind field from single-Doppler radar data. *J. Atmos. Sci.,* **51,** 2664–2682.

Liou, Y., 1999: Single radar recovery of cross-beam wind components using a modified moving frame of reference technique. *J. Atmos. Oceanic Technol.,* **16,** 1003–1016.

——, 2002: An explanation of the wind speed underestimation obtained from a least squares type of single-Doppler radar velocity retrieval method. *J. Appl. Meteor.,* **41,** 1216–1226.

Liu, S, and C. Qiu, 2003: A scheme to deal with non-simultaneous Doppler radar observation during three-dimensional wind field retrieval. *Plateau Meteor.,* **22,** 329–336.

Matejka, T., 2002: Estimating the most steady frame of reference from Doppler radar data. *J. Atmos. Oceanic Technol.,* **19,** 1035–1048.

Mewes, T., and A. Shapiro, 2002: Use of the vorticity equation in dual-Doppler analysis of the vertical velocity field. *J. Atmos. Oceanic Technol.,* **19,** 543–567.

Protat, A., and I. Zawadzki, 1999: A variational method for real-time retrieval of three-dimensional wind field from multiple-Doppler bistatic radar network data. *J. Atmos. Oceanic Technol.,* **16,** 432–449.

——, and ——, 2000: Optimization of dynamic retrievals from a multiple-Doppler radar network. *J. Atmos. Oceanic Technol.,* **17,** 753–760.

Qiu, C.-J., and Q. Xu, 1996: Least squares retrieval of microburst winds from single-Doppler radar data. *Mon. Wea. Rev.,* **124,** 1132–1144.

Scialom, G., and Y. Lemaître, 1990: A new analysis for the retrieval of three-dimensional mesoscale wind fields from multiple Doppler radar. *J. Atmos. Oceanic Technol.,* **7,** 640–665.

Shapiro, A., S. Ellis, and J. Shaw, 1995: Single-Doppler velocity retrievals with Phoenix II data: Clear air and microburst wind retrievals in the planetary boundary layer. *J. Atmos. Sci.,* **52,** 1265–1287.

Sun, J., and N. A. Crook, 1994: Wind and thermodynamic retrieval from single-Doppler measurements of a gust front observed during Phoenix II. *Mon. Wea. Rev.,* **122,** 1075–1091.

——, and ——, 1996: Comparison of thermodynamic retrieval by the adjoint method with the traditional retrieval method. *Mon. Wea. Rev.,* **124,** 308–324.

Tabary, P., and G. Scialom, 2001: MANDOP analysis over complex orography in the context of the MAP Experiment. *J. Atmos. Oceanic Technol.,* **18,** 1293–1314.

Weygandt, S. S., A. Shapiro, and K. K. Droegemeier, 2002: Retrieval of model initial fields from single-Doppler observations of a supercell thunderstorm. Part II: Thermodynamic retrieval and numerical prediction. *Mon. Wea. Rev.,* **130,** 454–476.

Xu, Q., and J. Gong, 2003: Background error covariance functions for Doppler radial-wind analysis. *Quart. J. Roy. Meteor. Soc.,* **129,** 1703–1720.

——, C. Qiu, and J. Yu, 1994: Adjoint-method retrievals of low-altitude wind fields from single-Doppler reflectivity measured during Phoenix II. *J. Atmos. Oceanic Technol.,* **11,** 275–288.

——, H. Gu, and C. Qiu, 2001: Simple adjoint retrievals of wet-microburst winds and gust-front winds from single-Doppler radar data. *J. Appl. Meteor.,* **40,** 1485–1499.

——, L. Wang, and N. Kang, 2003: Error covariance estimation for Doppler wind data assimilation. Preprints, *31th Conf. on Radar Meteorology,* Seattle, WA, Amer. Meteor. Soc., 108–109.

Xue, M., K. K. Droegemeier, V. Wong, A. Shaprio, and K. Brewster, 1995: Advanced Regional Prediction System (APPS) version 4.0 user's guide. 380 pp. [Available from Center for Analysis and Prediction of Storms, University of Oklahoma, 100 E. Boyd, Norman, OK 73019.]

Yang, S., and Q. Xu, 1996: Statistical errors in variational data assimilation—A theoretical one-dimensional analysis applied to Doppler wind retrieval. *J. Atmos. Sci.,* **53,** 2563–2577.

Zhang, J., and T. Gal-Chen, 1996: Single-Doppler wind retrieval in the moving frame of reference. *J. Atmos. Sci.,* **53,** 2609–2623.